Autoinflammatory periodic fever, immunodeficiency, and thrombocytopenia (PFIT) caused by mutation in actin-regulatory gene *WDR1*

Ariane S.I. Standing,[1,2]* Dessislava Malinova,[1]* Ying Hong,[1] Julien Record,[1] Dale Moulding,[1] Michael P. Blundell,[1] Karolin Nowak,[1] Hannah Jones,[1] Ebun Omoyinmi,[1] Kimberly C. Gilmour,[4] Alan Medlar,[3] Horia Stanescu,[3] Robert Kleta,[1,3,4] Glenn Anderson,[4] Sira Nanthapisal,[1] Sonia Melo Gomes,[1] Nigel Klein,[1] Despina Eleftheriou,[1] Adrian J. Thrasher,[1] and Paul A. Brogan[1]

[1]University College London Institute of Child Health, London WC1E 6BT, England, UK
[2]Institute of Biomedical and Environmental Science and Technology, University of Bedfordshire, Luton LU2 8DL, England, UK
[3]University College London Division of Medicine, London WC1E 6BT, England, UK
[4]Great Ormond Street Hospital for Children NHS Foundation Trust, London WC1N 3JH, England, UK

The importance of actin dynamics in the activation of the inflammasome is becoming increasingly apparent. IL-1β, which is activated by the inflammasome, is known to be central to the pathogenesis of many monogenic autoinflammatory diseases. However, evidence from an autoinflammatory murine model indicates that IL-18, the other cytokine triggered by inflammasome activity, is important in its own right. In this model, autoinflammation was caused by mutation in the actin regulatory gene *WDR1*. We report a homozygous missense mutation in *WDR1* in two siblings causing periodic fevers with immunodeficiency and thrombocytopenia. We found impaired actin dynamics in patient immune cells. Patients had high serum levels of IL-18, without a corresponding increase in IL-18–binding protein or IL-1β, and their cells also secreted more IL-18 but not IL-1β in culture. We found increased caspase-1 cleavage within patient monocytes indicative of increased inflammasome activity. We transfected HEK293T cells with pyrin and wild-type and mutated *WDR1*. Mutant protein formed aggregates that appeared to accumulate pyrin; this could potentially precipitate inflammasome assembly. We have extended the findings from the mouse model to highlight the importance of WDR1 and actin regulation in the activation of the inflammasome, and in human autoinflammation.

INTRODUCTION

The actin cytoskeleton is crucial for normal immune function, and a growing number of primary immunodeficiencies are caused by mutations in actin-regulating genes (Moulding et al., 2013). Autoinflammatory diseases (AIDs) are defined as diseases predominantly of the innate immune system resulting in abnormally increased inflammation (Standing et al., 2013), and it is recognized that autoinflammation and immunodeficiency may coexist (Frenkel, 2014). Recently, a new AID has been described in mice (*WDR1*$^{rd/rd}$ mouse), caused by recessive mutation in *WDR1* (Kile et al., 2007; Kim et al., 2015), a WD40 repeat protein that interacts with cofilin to promote F-actin severing and depolymerization (Okada et al., 1999, 2002; Rodal et al., 1999; Ono et al., 2004). Autoinflammation in the *WDR1*$^{rd/rd}$ mouse is caused by excessive IL-18 production by monocytes, and not by IL-1β. This dysregulated monocytic IL-18 secretion requires caspase-1, apoptosis-associated speck-like protein containing a caspase recruitment domain (ASC), and pyrin (Kim et al., 2015). In this study, we have identified a family with severe autoinflammatory disease with many features in common with the murine disease, and harboring a variant in *WDR1*.

RESULTS AND DISCUSSION

Two Pakistani girls (patients IV-2 and IV-4; Fig. 1 A) born of consanguineous parents suffered from a severe AID beginning in the first weeks of life. Both had periodic fevers lasting 3–7 d, every 6–12 wk, with severe acute phase responses: C-reactive protein, >270 mg/liter (reference range [RR] < 20); serum Amyloid A, >200 mg/liter (RR < 10); leukocytosis, 32 × 10^9/liter (predominantly neutrophils); hyperferritinaemia, 82–2,679 µg/ml (RR 11–76); and thrombocytopenia, 24–90 × 10^9/liter; as well as normalization of these parameters in

*A.S.I. Standing and D. Malinova contributed equally to this paper.

Correspondence to Ariane Standing: ariane.standing@ucl.ac.uk

Abbreviations used: AID, autoinflammatory disease; CAPS, cryopyrin-associated periodic syndrome; CRP, C-reactive protein; EBV, Epstein-Barr virus; HSCT, hematopoietic stem cell transplantation; moDC, monocyte-derived DC; MPV, mean platelet volume; PFIT, periodic fevers, immunodeficiency, and thrombocytopenia; PHA, phytohemagglutinin; sJIA, systemic juvenile idiopathic arthritis.

The Rockefeller University Press $30.00
J. Exp. Med. 2017 Vol. 214 No. 1 59–71
https://doi.org/10.1084/jem.20161228

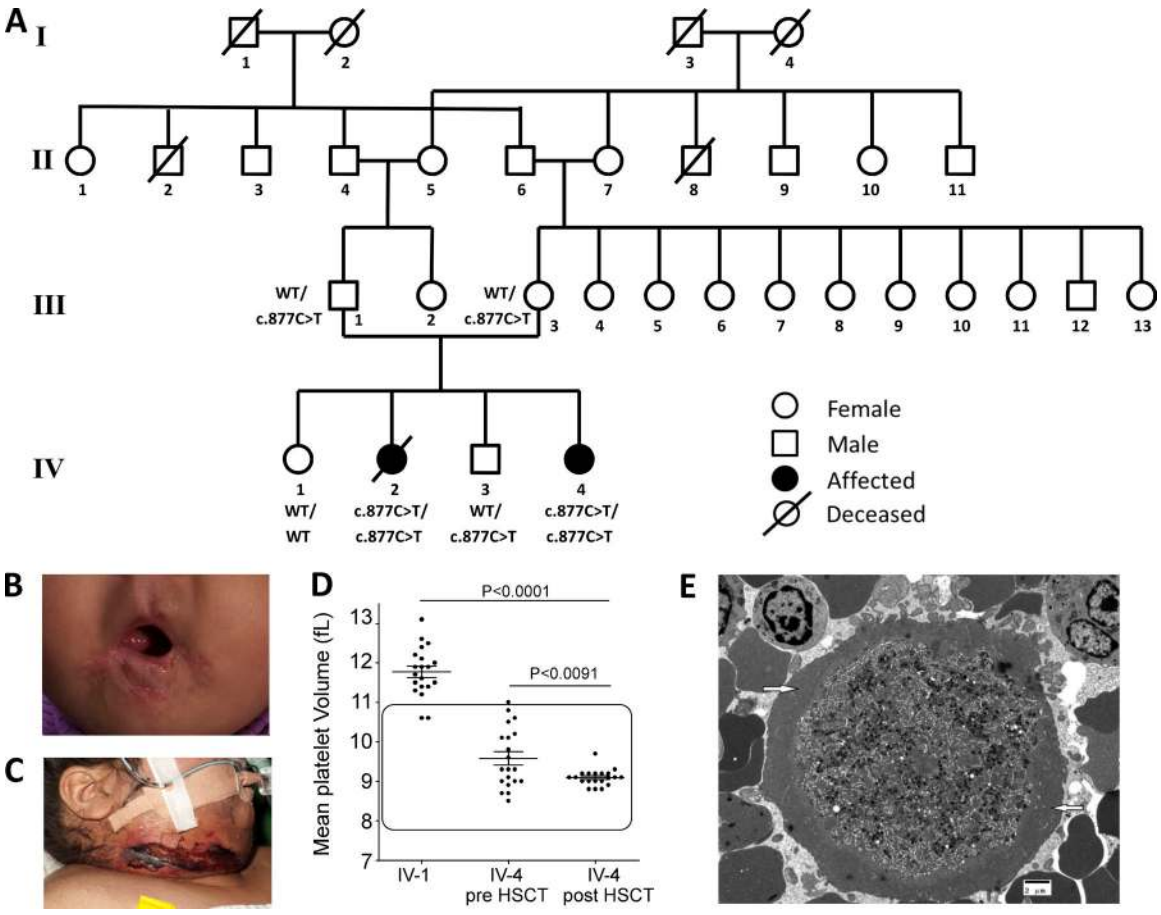

Figure 1. **Clinical features and results of genetic analyses in the family.** The family pedigree (A) shows the two affected female siblings, and their two unaffected siblings from consanguineous marriage of double first cousins; segregation of the c.877C>T *WDR1* variant is also shown. Acquired microstomia (B) in patient IV-2 aged 12 yr and 10 mo, the consequence of recurrent sterile oral inflammatory episodes. At 13 yr of age, patient IV-2 developed a severe necrotizing cellulitis of the neck caused by *Streptococcus pneumoniae* (C). (D) Mean platelet volume (fl) derived from a standard complete blood count using a Beckman Coulter counter. Normal reference range (7.8–11 fl) is denoted by the gray shaded area. Data are 20 random measurements taken as routine clinical care; horizontal lines denote mean and SEM. Patient IV-2 had mean MPV consistently greater than the reference range (with the exception of two measurements: mean MPV, 11.77 fl; range, 10.6–13.10), and significantly higher than her sibling both before and after HSCT ($P < 0.0001$, ANOVA). Patient IV-4 had MPV consistently within normal range (mean, 9.58 fl; range, 8.50–11.00). However, MPV was significantly lower after HSCT ($P = 0.0091$, nonpaired Student's *t* test). Transmission electron microscopy of megakaryocytes in a bone marrow aspirate before allogeneic HSCT in patient IV-4 (E) revealed occasional small, atypical megakaryocytes with no nucleus and failure of the demarcating membrane system to develop resulting in a large peripheral zone (arrows) devoid of organelles and granules. Developing platelets were located in the central area of the cell.

between fever attacks. Both had severe recurrent oral inflammation, which caused scarring and acquired microstomia in patient IV-2 (Fig. 1 B), and recurrent perianal ulceration. Genetic screening for common AIDs (*TNFRSF1A*, *MVK*, *NLRP3*, and *MEFV*) was negative. Frequent infections were also observed even before immunosuppression. Patient IV-4 developed *Pneumocystis jiroveci* pneumonia at 5 mo of age; and *Staphylococcus aureus* septic arthritis of the knee at 2 yr of age. Patient IV-2 developed *Streptococcus pneumonia* necrotizing cellulitis 13 yr of age (Fig. 1 C). Both developed severe inflammatory responses to (presumed) viral infections, with moderate thrombocytopenia. Mean platelet volume (MPV) was elevated in patient IV-2, but within normal range for IV-4 (Fig. 1 D). Bone marrow aspirate in patient IV-4 revealed ultrastructural abnormalities of megakaryocytes by electron microscopy (Fig. 1 E). Detailed immunological work-up of both children excluded autoimmunity, common primary immunodeficiency syndromes, and primary hemophagocytic lymphohistiocytosis (Table S1). In patient IV-4, phytohemagglutinin (PHA) stimulation of T cells was normal, but T cell activation in response to stimulation with anti-CD3 was diminished, implicating a defect in adaptive immunity. Patient IV-2 had normal T cell activation to PHA, but T cell activation in response to anti-CD3 was not documented. Neutrophil respiratory burst and phagocytosis of opsonized *Escherichia coli* (in IV-4) were normal.

Both children partially responded to corticosteroids, and to colchicine, but poor growth and inflammatory attacks persisted. Patient IV-2 failed several antiinflammatory and immunosuppressive agents (Table S1). There was, however, some transient steroid sparing effect in response to anakinra (2–4 mg/kg s.c. daily). Ultimately, however, this did not control the episodes of autoinflammation, and this patient died at 14 yr of age from sterile systemic inflammation and multiorgan failure. Patient IV-4 successfully underwent allogeneic hematopoietic stem cell transplantation (HSCT) at age 8, and remains well, off all medication, 3 yr later.

We used exome sequencing combined with homozygosity mapping to investigate the genetic cause. Regions of homozygosity are provided in Table S2. We confirmed that there were no further variants of interest in any known autoinflammatory genes in the INFEVERS database (Sarrauste de Menthière et al., 2003) or HLH genes (Bode et al., 2012), including *NLRC4* (Canna et al., 2014), nor in genes that could generate increased IgA levels, such as CD40L or NEMO (Allen et al., 1993; Orange et al., 2004). On chromosome 4, a homozygous mutation was identified in *WDR1* through exome sequencing, which has not been reported in dbSNP or the exome sequencing project databases. This missense mutation affects both transcripts of the gene: transcript 1 exon 8 c.877C>T, amino acid change L293F and transcript 2 exon 5 c.457C>T, amino acid change L153F are predicted to be damaging by PolyPhen2 (Adzhubei et al., 2010) and MutationTaster (Schwarz et al., 2010) and segregated with disease (Fig. 1 A). The protein comprises 14 WD40 repeats, which are organized into two propellers with seven blades each (Fig. 2 A; Mohri et al., 2004). The mutation is predicted to disrupt intramolecular hydrophobic interactions, which are important for maintaining protein structure (Fig. 2, B–E).

The cofilin–WDR1 complex facilitates breakdown of existing filaments while promoting increased F-actin polymerization from newly created barbed ends, and is thus pivotal in the maintenance of cytoskeletal integrity and function (Rodal et al., 1999). In the *WDR1*$^{rd/rd}$ mouse, neutrophils and macrophages showed increased levels of polymerized actin compared with wild-type. Phalloidin staining and flow cytometry of monocyte-derived DCs (moDCs), $CD14^-$ lymphocytes, and Epstein-Barr virus (EBV)–transformed lymphoblasts from IV-4 demonstrated increased levels of polymerized F-actin relative to control (Fig. 3 A). Confocal microscopy confirmed more intense F-actin–rich podosome staining and abnormal intracellular aggregates of WDR1 in patient moDCs (Fig. 3 B). Although the number of podosomes was similar, the volume of patient IV-4's podosomes was greater than control (Fig. 3 C). Podosomes are cellular adhesion structures involved in matrix degradation and invasion, containing an F-actin core and a ring of cytoskeletal adaptor proteins, including WDR1 (Cervero et al., 2012). Increased podosome volumes observed here are consistent with diminished F-actin depolymerization caused by defective *WDR1*.

In an attempt to model this, we transduced the THP1 monocytic cell line with shRNA against *WDR1* or with a scrambled control. We produced two cell lines with different shRNA sequences that showed negligible *WDR1* expression compared with untransduced cells and scrambled control. However, these cells showed no difference in actin polymerization assessed by flow cytometry (Fig. S2 F). This phenomenon has been reported previously; depleted WDR1 levels may lead to up-regulation of caspase 11 and cofilin, to partially rescue the defect (Li et al., 2007; Okreglak and Drubin, 2007). Furthermore, In the *WDR1*$^{rd/rd}$ mouse the protein is also misfolded (Kile et al., 2007), thus mutant rather than absent WDR1 is likely required for the autoinflammatory phenotype.

Autoinflammation in the *WDR1*$^{rd/rd}$ mouse is driven by IL-18 independently of IL-1β. IL-1β and IL-18 are activated by inflammasomes, and have both overlapping and divergent roles (Brydges et al., 2013). Sera from both patients taken at three to five time points over 5–7 mo (preHSCT) demonstrated no change in IL-1β compared with healthy childhood controls (Fig. 4 A), but did have elevated IL-18 levels, which were higher than levels detected in systemic juvenile idiopathic arthritis (sJIA) patients (Fig. 4 B; Chen et al., 2013). In contrast to the sJIA patients, however, levels of IL-18–binding protein (IL-18BP) were not elevated (Fig. 4 C). IL-18BP neutralizes the proinflammatory activity of IL-18, thus the low levels observed may contribute to the autoinflammatory phenotype (Chen et al., 2013; Dinarello et al., 2013). IL-18 levels mirrored SAA and C-reactive protein (CRP) levels in IV-2, who was on anakinra when samples were taken (Fig. 4 D), and were persistently elevated in IV-4 (not on anakinra; Fig. 4 E). Although there was partial efficacy of anakinra in IV-2 that could suggest a role for IL-1β in the human disease, we are intrigued by recent suggestions that anakinra may also partially antagonize IL-18 (Brydges et al., 2013; Vastert et al., 2014). IL-1β levels are usually low in serum, even in IL-1β–mediated diseases, as it often acts locally and degrades rapidly. Therefore we also investigated IL-1β and IL-18 production from the cultured moDCs treated with LPS for 4 h. We detected elevated IL-18 production, but not IL-1β, from patient cells (Fig. 4, G and H) in response to LPS. As before, polymerized F-actin levels were assessed using flow cytometry. Untreated moDCs from patient IV-4 had 1.3-fold F-actin intensity versus control, rising to 1.8-fold after LPS treatment (Fig. 4 I). We also detected significantly increased IL-18 production from cultured neutrophils from IV-4 compared with control when stimulated with LPS, but not in response to other experimental conditions (Fig. 4 J). The neutrophil defects in these patients appeared relatively mild, as respiratory burst and phagocytosis were normal (Table S1). We further assessed neutrophil migratory function from patient IV-4 using a modified Dunn chamber, and found no significant difference in velocity or chemotactic index (Fig. 5, A–C). Thus, alteration in neutrophil function alone is unlikely to account for the full disease phenotype. Although neutrophil chemotaxis was reduced, the presence of functional immunodeficiency was not fully evaluated in the *WDR1*$^{rd/rd}$ mouse,

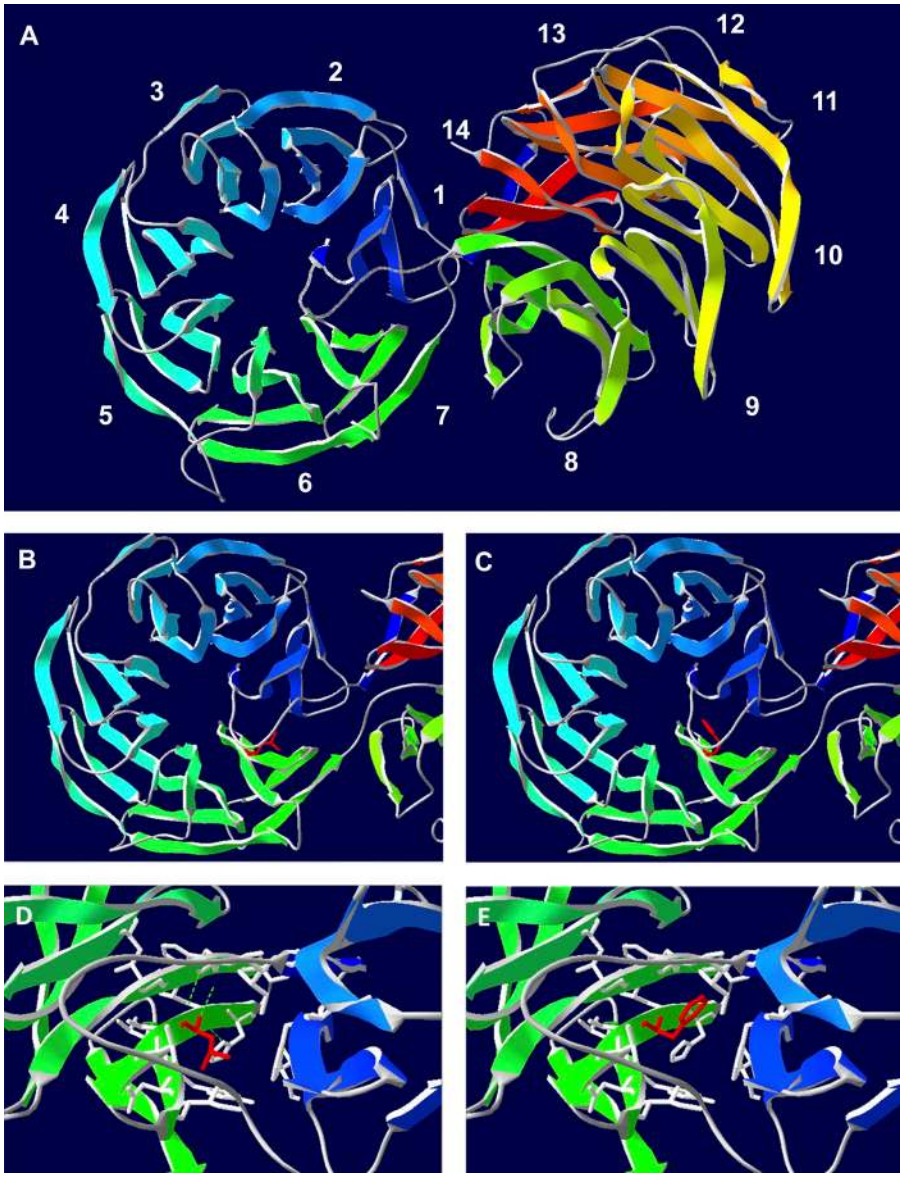

Figure 2. **Protein structure of WDR1 and predicted effect of L293F mutation.** The WDR1 pdb file was downloaded from exPASY, and protein was viewed and manipulated with the Swiss PDB viewer. (A) The protein chain is colored from blue at the initiation of the N terminus of the protein to red. The two propellers are labeled N and C, and the blades are numbered 1–14. (B) A close up of the N-terminal propeller showing the leucine residue side chain in red in blade 7, close to blade 1; and (C) the residue mutated to phenylalanine. Predicted H bonds with neighboring residues are shown (D) for leucine and (E) for phenylalanine. The L293F amino acid change occurs in blade 7 close to the tail of the N-terminal propeller, where the protein strand feeds into the join with the C-terminal propeller. Hydrophobic interactions between blade 1 and 7 are important for closing the circular propeller structure of this domain (Mohri et al., 2004). Each propeller blade is composed of four anti-parallel β-sheets; in the wild-type protein, the leucine residue at position 293 is predicted to form three hydrogen bonds supporting this structure (D). Mutating this residue to a phenylalanine disrupts these bonds (E), with predicted functional consequences, as the two propellers mediate protein–protein interactions. Residues in the N terminus are important for F-actin binding and disassembly (Mohri et al., 2004), whereas the C terminus interacts with the CARD domain of murine caspase-11 (a homologue of human caspases 4 and 5; Li et al., 2007).

as mice were kept in a relatively protected environment (Kile et al., 2007; Kim et al., 2015). The ability of moDCs from patient IV-4 to phagocytose and process uncapsulated *Neisseria meningitidis* (an actin-mediated process; Jones et al., 2008) was reduced (Fig. 5 D), suggesting that the phagocytic defect may not affect all phagocytic cell types to the same extent, and may reflect a defect in the subsequent processing of antigen for presentation in DCs (Savina and Amigorena, 2007).

Immunodeficiency in these patients is likely to be multifactorial, given the manifold roles that podosomes and actin play in the immune system. Similar to Wiskott-Aldrich syndrome, we observed a diminished T cell proliferative response to aCD3 stimulation, but intact PHA response (Dupré et al., 2002; Sasahara et al., 2002; Bouma et al., 2011; Calvez et al., 2011; Malinova et al., 2016). This may not be surprising, given the importance of force generation for T cell activation, and thus expected involvement of the actin cytoskeleton (Hu and Butte, 2016).

Given that IL-18 activation in the *WDR1*$^{rd/rd}$ mouse is dependent on the pyrin inflammasome (Kim et al., 2015), we hypothesize that pyrin also interacts with WDR1 through its CARD domain. Murine caspase 11 (equivalent to human caspases 4 and 5) expression is induced by LPS and then binds WDR1 to recruit cofilin and trigger F-actin depolymerization through a CARD domain (Li et al., 2007). Caspases 4, 5 and 11 can be activated by binding LPS directly, again through the CARD domains (Hagar et al., 2013; Shi et al., 2014). Pyrin and the ASC complex have previously been reported to directly interact with polymerized actin (Waite et al., 2009), and pyrin detects the Rho GTPase, modifying activity of bacterial toxins through downstream changes in the actin cytoskeleton and subsequently activates the pyrin inflammasome (Flanna-

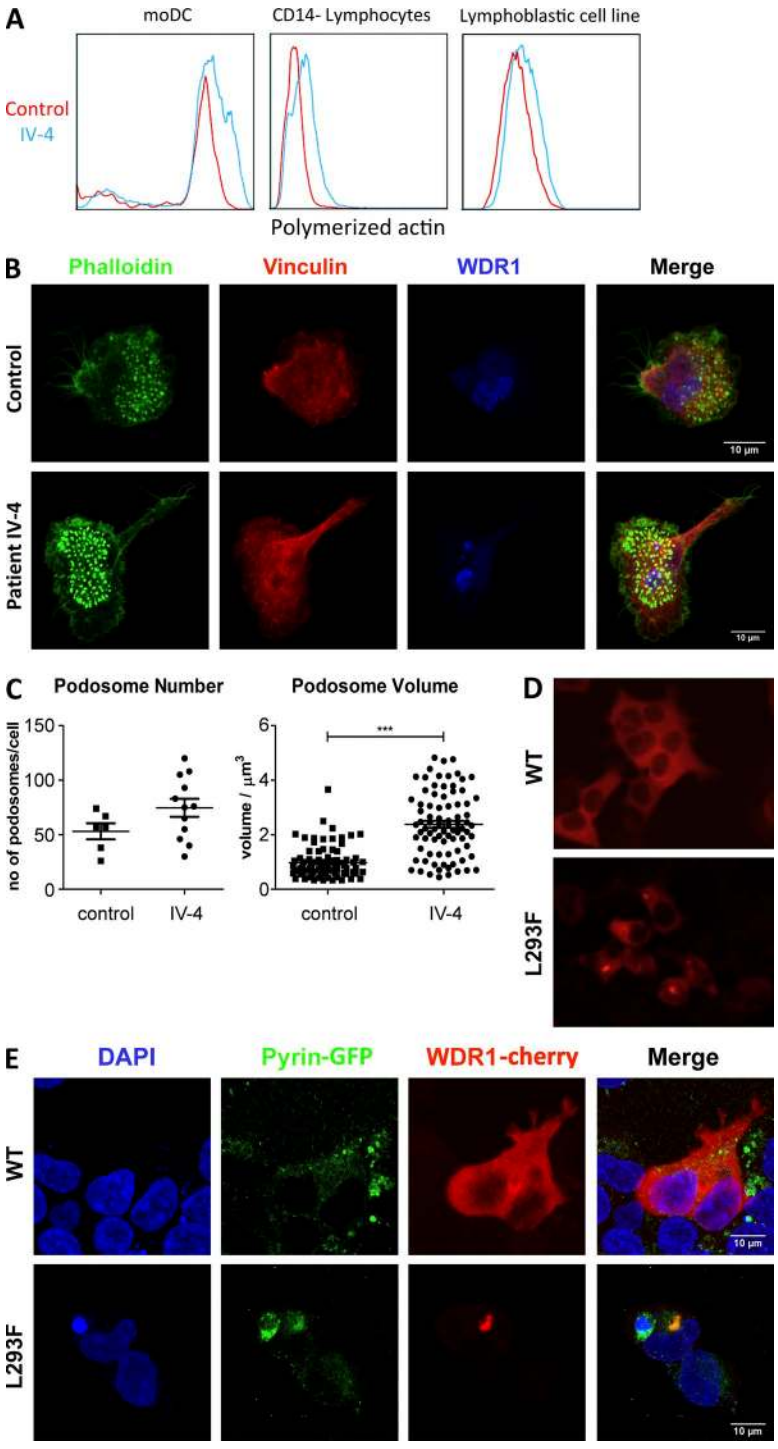

Figure 3. **F-actin levels and WDR1 expression in patient and HEK293T cells.** (A) Representative phalloidin staining of polymerized F-actin of cells from patient IV-4 (blue) and control cells (red) using flow cytometry revealed increased F-actin in moDCs (n = 3), $CD14^-$ lymphocytes (n = 1), and immortalized lymphoblasts from patient IV-4 compared with control (measured three times, compared with three controls). (B) Confocal microscopy of moDCs from patient IV-4 and a healthy control stained with phalloidin (green), anti-vinculin (red), and anti-WDR1 (blue) revealed aberrant localization of WDR1 and bright staining of podosomes in cells from patient IV-4, performed once as patients underwent HSCT. Additional images are provided in Fig. S1 A. (C) Analysis of the podosomes with Volocity software indicated that although podosome number did not differ significantly between patient IV-4 and control (P = 0.1145, two-tailed unpaired Student's t test), podosome volume was significantly larger in patient IV-4 (***, P < 0.001; two-tailed unpaired Student's t test; error bars represent the SEM). (D) *WDR1* mRNA was cloned from patient IV-4 or control, fused to the mCherry reporter, and expressed in HEK293T cells. Mutant WDR1 produced from the patient mRNA formed aggregates with markedly different intracellular appearance compared with cells transfected with healthy control *WDR1* mRNA. (E) When cotransfected with GFP-pyrin, the pyrin also localized to these WDR1 aggregates. Additional images provided in Fig. S1 B.

gan et al., 2012; Gavrilin et al., 2012; Rosales-Reyes et al., 2012; Xu et al., 2014). We speculate that WDR1 protein may be part of the link between these events. To begin to assess this, we cloned *WDR1* mRNA from IV-4 or a healthy control into a pmCherry-N1 vector and transfected HEK293T cells. Although WT-*WDR1*-mCherry exhibited a uniform distribution, the L293F-*WDR1*-mCherry formed abnormal intense aggregates (Fig. 3 D) similar to those we observed in the patient moDCs (Fig.3B). We then studied co-localization of mutant or WT WDR1 with pyrin by co-transfection with pyrin-GFP. When introduced in the presence of L293F-*WDR1*-mCherry, we confirmed that pyrin co-localized with mutant WDR1 aggregates (Fig. 3 E). We speculate that this interaction may trigger spontaneous ASC speck formation,

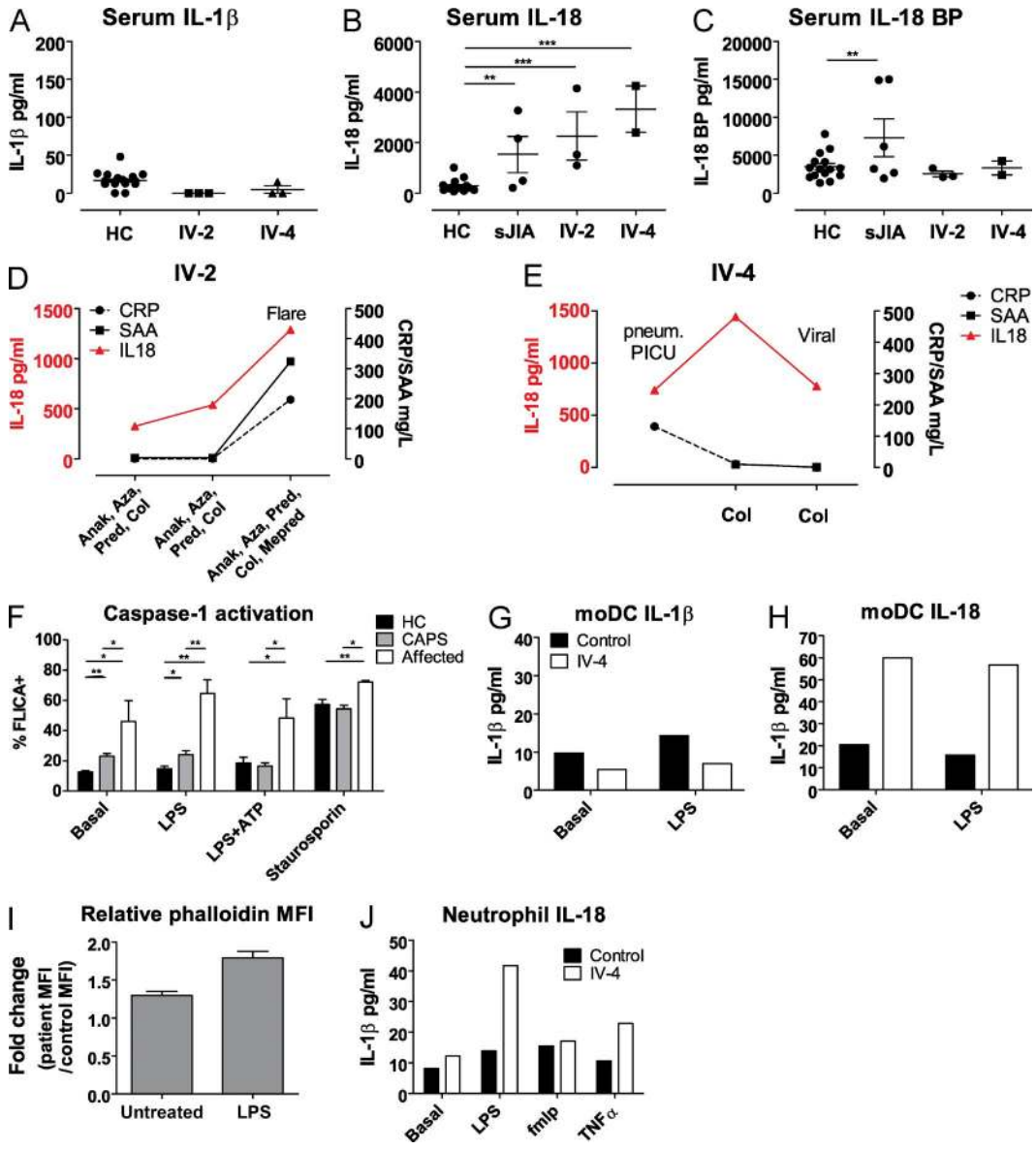

Figure 4. **Cytokine levels in sera and in vitro stimulation of patient cells.** (A) IL1β was not significantly elevated in either patient compared with sera from healthy pediatric controls when measured on three separate occasions over several months. (B) In contrast, IL-18 was significantly increased in both patients (***, $P < 0.0001$, two-tailed unpaired Student's *t* test for both). IL-18 was also significantly elevated in the serum of sJIA patients ($n = 6$) compared with controls (**, $P = 0.0023$, two-tailed unpaired Student's *t* test) who also showed increased levels of IL-18BP in the same samples ($P = 0.0343$, two-tailed unpaired Student's *t* test), which was not observed in either patient (C). (D) In patient IV-2, IL-18 mirrored CRP and serum amyloid A (SAA) levels; but was persistently elevated in IV-4, even when CRP and SAA were normal (E; IL-18 measured by ELISA). (F) Caspase-1 activation, measured as the proportion of FLICA$^+$ cells by flow cytometry was significantly elevated in CD14$^+$ cells from both patients ($n = 2$) compared with controls ($n = 4$) and CAPS patients ($n = 5$) at baseline and after stimulation with LPS and staurosporine (*, $P < 0.05$; **, $P < 0.01$, two-tailed unpaired Student's *t* tests). (G) IL-1β levels produced by moDCs after 4 h at baseline or upon treatment with LPS showed little difference between cells from control and patient IV-4, but IL-18 levels in the same supernatant were much higher in patient IV-4 (H). Experiment was performed once, as patient cells were limited because this patient underwent HSCT. (I) In the moDCs from this same experiment, the relative amount of polymerized F-actin in these same moDCs from patient IV-4 was higher compared with control moDCs, and increased even further upon stimulation with LPS (error bars represent experimental replicates from reciprocal staining with CFSE). (J) IL-18 production from neutrophils from patient IV-4 and control at baseline and after treatment with LPS, *N*-formylmethionyl-leucyl-phenylalanine (FMLP) and TNF. LPS stimulated greater IL-18 production from neutrophils from patient IV-4 (experiment performed once, again due to limited availability of cells from this patient). Error bars in each panel indicate SEM. Anak, Anakinra; ATP, adenosine triphosphate Aza, azathioprine; Col, colchicine; HC, healthy control; IL-18 BP, IL-18–binding protein; Mepred, methylprednisolone; MFI, median fluorescence index; Pred, prednisolone; SAA, serum amyloid A.

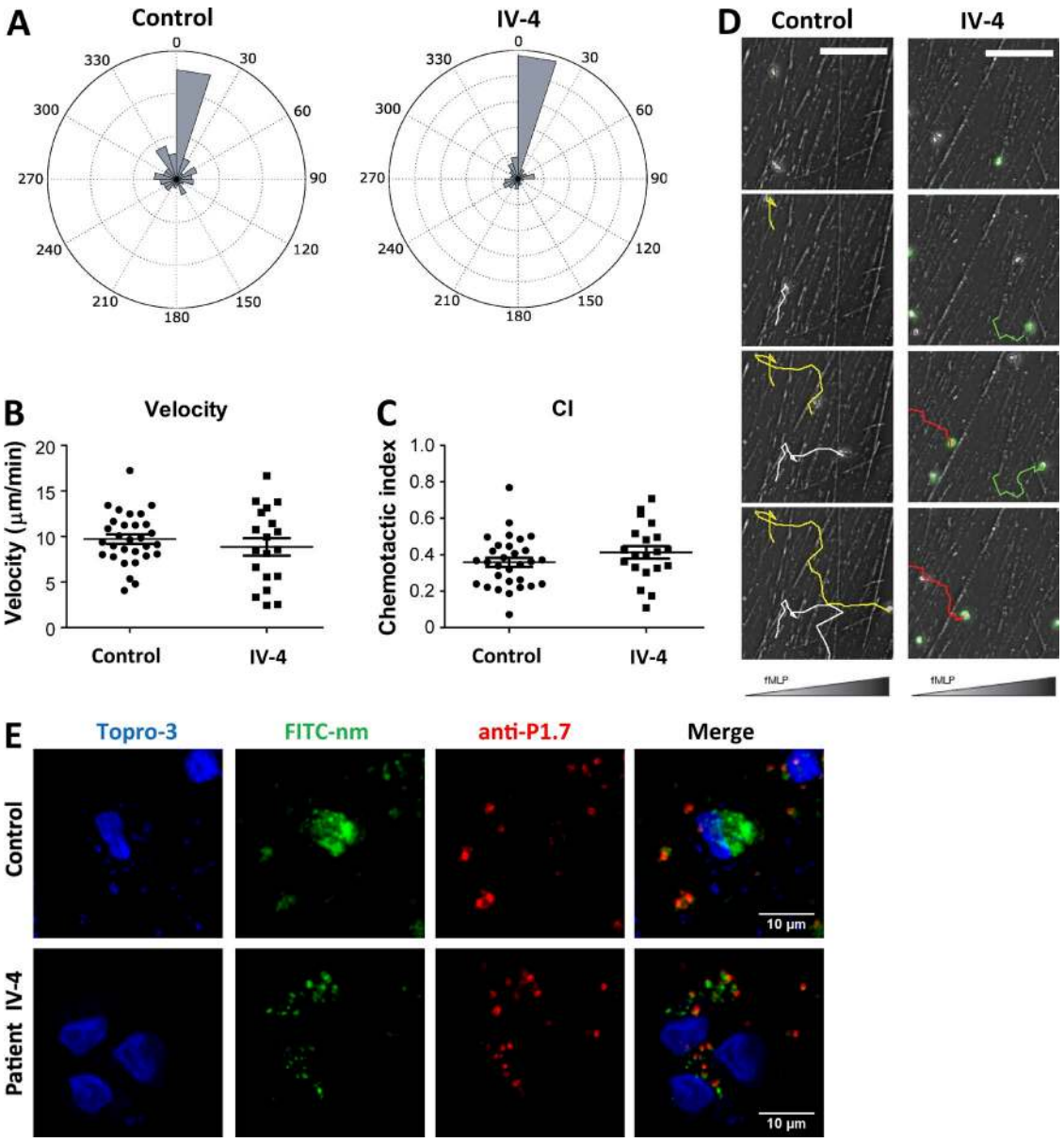

Figure 5. **Migratory capacity of neutrophils and phagocytosis of uncapsulated *N. meningitidis* by moDCs.** Neutrophils isolated from patient IV-4 and control showed no significant difference in migratory capacity in regards to instantaneous angle of migration (A), velocity (B), or chemotactic index (C). Experiment performed once as patients underwent HSCT. Example traces of migrating cells are shown in D. Bar, 100 µm. (E) Patient IV-4 and control moDCs were incubated with FITC-labeled uncapsulated *N. meningitidis* (FITC-nm; green). After 4 h, cells were fixed and labeled with TOPRO-3 nuclear stain (blue), and anti-P1.7 antibodies (red) which only labels the surface of any bacteria external to the cells, thus identifying bacteria that have not been phagocytosed. After 4 h, control cells had phagocytosed nearly all the FITC-nm and transported them adjacent to the nucleus, whereas fewer of the patient moDCs had completed this process. The mean proportion of control moDCs undergoing phagocytosis was 0.56 (SD = 0.18) versus 0.22 (SD = 0.11), performed once on moDCs from patient IV-4 ($P = 0.04$; unpaired *t* test).

activating the pyrin inflammasome. We investigated heterozygous family members and found no increase in polymerized phalloidin levels, inflammasome activation, or IL-18 production in their cells (Fig. S2). This confirms that the phenotype is recessive, even if this mutation has an activating component it cannot manifest without complete loss of wild-type protein function. We also do not have data on the comparative binding kinetics of wild-type and mutated protein and how they interact when both are present. This warrants further study in the future. Because activation of the pyrin inflammasome culminates in caspase-1 activation, we measured this using the FLICA assay and flow cytometry gating on $CD14^+$

cells from PBMCs, and found greater caspase-1 activation in both patients at baseline and after stimulation compared with healthy controls and patients with cryopyrin-associated periodic syndrome (CAPS), who are known to have spontaneous NLRP3-inflammasome activation and high caspase-1 (Fig. 4 F). Similar to the murine model, these results confirm that caspase-1 activation and elevated IL-18 are likely to be central to the pathogenesis of autoinflammation in humans caused by mutated WDR1 protein.

We observed ultrastructural abnormalities of megakaryocytes in patient IV-4 (Fig. 1 D), revealing occasional small, atypical megakaryocytes, with no nucleus and failure of the development of the demarcating membrane system. The thrombocytopenia we observed could thus be explained by dysfunctional platelet shedding, because WDR1 is required for megakaryocyte maturation and platelet shedding in the *WDR1*$^{rd/rd}$ mouse (Kile et al., 2007).

In conclusion, homozygous missense L153F/L293F mutation in the actin regulatory gene *WDR1* causes a new AID in humans, with periodic fevers, immunodeficiency, and intermittent thrombocytopenia (PFIT). The human disease resembles the murine *WDR1*$^{rd/rd}$ mouse model caused by hypomorphic recessive *WDR1* mutations (Kile et al., 2007; Kim et al., 2015), and this highlights a potentially crucial link between the actin cytoskeleton and autoinflammation. New questions now arise regarding the precise molecular mechanisms governing WDR1 activity and the human PFIT phenotype. Although we cannot yet conclude that PFIT is driven purely by IL-18, our data do suggest an important role for this proinflammatory cytokine, driven by caspase-1 activation. Targeted IL-18 blockade, if available, might have been a more effective strategy to treat the autoinflammatory component of the disease. In the *WDR1*$^{rd/rd}$ mouse, transplant of bone marrow cells from wild-type mice corrected the autoinflammatory phenotype and macrothrombocytopenia; the same appears to be true in PFIT, as allogeneic HSCT cured patient IV-4. Given that severe autoinflammation coexists with immunodeficiency and thrombocytopenia in PFIT, for the time being, we suggest that HSCT is the most appropriate treatment.

MATERIALS AND METHODS

Experiments

This study was approved by the Bloomsbury ethics committee (ethics number 08H071382); we obtained written informed consent from all the family members and controls who participated. In vitro studies were performed in CD14$^+$ moDCs, CD14$^-$ lymphocytes, neutrophils, and EBV immortalized B cells from patients and controls. Confocal microscopy was performed in HEK293T cells transfected with *WDR1* cloned from the mRNA of patient IV-4 or of a healthy WT control, and fused to the mCherry reporter; and with GFP-pyrin.

Granule release assay

The granule release assay was performed according to Wheeler et al. (2010). PBMCs were stimulated with IL-2 overnight, and then incubated with FITC-conjugated anti-CD107a antibody alone, or with anti-CD3 antibody or PHA, for 2 h. Samples were analyzed by flow cytometry and gating on lymphocytes by forward/side scatter. CD107a expression was analyzed on cytotoxic T cells (CD8$^+$ and CD3$^+$) and on NK cells (CD56$^+$ and CD3$^-$), and the increase in percentage of CD107a$^+$ cells between unstimulated and stimulated samples was calculated.

PHA and CD3 stimulation

PHA stimulation. Whole blood was stimulated with PHA (Inverness Medical), which preferentially stimulates T helper (CD4) cells via the IL-2 receptor, to assess an immune response. The blood was diluted 1:20 with RPMI-1640 (Life Technologies). 200 µl of cell suspension was pipetted into 10 wells. The first two wells were untreated; the remaining eight wells had PHA added to duplicate wells in concentrations of 1, 2, 4, and 8 µg/ml. The plate was incubated at 37°C with 5% CO_2 for 4 or 3 d.

CD3 stimulation. Lymphocytes were separated from whole blood using lymphoprep (Alere), and the cells were then cultured at a concentration of 10^6/ml with 10% AB serum in RPMI with and without anti-CD3 at a final concentration of 0.3 µg/ml (eBioscience) in triplicate, then incubated at 37°C with 5% CO_2 for 4 d.

For both assays to measure the proliferation, 10 µl (1 µCur) of tritiated thymidine (PerkinElmer) was added to each of the wells, and the plate was returned to the incubator for 4 h. Any actively dividing cells incorporated the tritiated thymidine. The plates were then harvested (FilterMate cell harvester; PerkinElmer) and the radioactivity was counted using the β counter (TopCount β counter; PerkinElmer). The amount of proliferation was demonstrated by the amount of tritiated thymidine incorporation into the cells measured by CPM on the β counter. Control samples were always set up alongside patient samples. For PHA stimulation, control results should be <400 CPM for 0 µg/ml PHA and >12,500 for the highest CPM. For CD3 stimulation, control results should be <600 CPM without anti-CD3 and >6,000 with anti-CD3.

Neutrophil phagocytosis assay

Neutrophil phagocytosis at 2, 5, and 10 min was analyzed in whole blood using the Glycotope Phagoburst Assay (BD) according to the manufacturer's instructions. A normal range was established using 50 healthy individuals, and a normal control was run with each sample.

Electron microscopy of bone marrow aspirate

EDTA bone marrow samples were centrifuged to form buffy coat preparations. These were fixed in 2.5% glutaraldehyde in 0.1 M cacodylate buffer, followed by secondary fixation in 1.0% osmium tetroxide. Samples were dehydrated in graded ethanol, transferred to propylene oxide, and then infiltrated and embedded in Agar 100 epoxy resin. Polym-

erization was at 60°C for 48 h. 90-nm ultrathin sections were cut using a Diatome diamond knife on a Leica Ultracut UCT ultramicrotome. Sections were picked up on copper grids and stained with alcoholic uranyl acetate and lead citrate. The samples were examined in a JEOL 1400 transmission electron microscope and images recorded using an AMT XR80 digital camera.

Genetic mapping and sequencing

200 ng genomic DNA from patients, siblings, and the parents was isothermally amplified and enzymatically fragmented before hybridization to Illumina Human610-Quad arrays overnight. These were imaged using the Illumina iScan. The regions of homozygosity were identified using Illumina's Beadstudio with the Loss of heterozygosity detector plug-in (version 1.0.3); the minimum number of contiguous homozygous SNPs was set to 100.

Whole-exome sequencing was completed using the TruSeq exome kit (version 2; Illumina) and sequenced on the HiSeq2000 (Illumina). The raw sequence data were aligned to the human reference genome using the Burrows-Wheeler Aligner (BWA) alignment algorithm. Variant calling was with the Genome Analysis ToolKit (GATK). Variant annotation was with ANNOVAR and SNPEFF.

The *WDR1* variant was confirmed and familial segregation ascertained by PCR and Sanger sequencing using the following primers to amplify and sequence exon 8 forward: 5′-ACTCTGGTCTCTTCCCTGTCC-3′ and reverse: 5′-TTTGGGGTCTCTCTCCAGTC-3′. Sequencing was completed with the AB3730 using the BigDye v3.1 kit (Applied Biosystems).

The WDR1 pdb file was downloaded from ExPASY, and protein was viewed and manipulated with Swiss PDB viewer.

PBMC and neutrophil separation

Blood was collected into Falcon tubes (Thermo Fisher Scientific) containing 35 U preservative-free heparin (CP Pharmaceuticals) per 50 ml. 2 ml of a 5% dextran-saline solution was added per 10 ml of blood and gently mixed by inversion before being left to sediment for 30 min. The plasma layer was collected and overlaid on an equal volume of Ficoll-Paque reagent, and then centrifuged 800 *g* for 10 min with the brake off. The PBMC layer was taken for $CD14^+$ cell selection, and the neutrophil pellet was resuspended in distilled water for 20 s before addition of 2× saline solution to restore isotonicity. The neutrophils were then centrifuged at 1,200 rpm for 7 min and resuspended in warm RPMI with 10% FCS.

Monocyte and lymphocyte separation

$CD14^+$ cells were magnetically labeled and positively selected on LS columns (Miltenyi Biotec). The $CD14^-$ lymphoctyes were collected in column flow-through. $CD14^+$ cells were eluted from the column for moDC generation.

moDC generation

$CD14^+$ cells were cultured in the presence of 10 ng/ml recombinant human IL-4 (rhIL-4) and 10 ng/ml recombinant human granulocyte-macrophage colony stimulating factor for 6 d. Cells were split on days 2 and 5, with addition of fresh cytokines. On day 6 or 7, both adherent and suspension cells were harvested for use.

B-lymphoblastoid cell lines (B-LCL) generation

EBV viral supernatant was produced from the B95-8 cell line, which releases high titers of transforming EBV. This virus was then used to establish human lymphoblastoid lines. In brief, on day 0, 2.5×10^7 B95-8 cells were suspended in 15 ml (1.67×10^6/ml) of RF10 (RPMI 1640 + 10% FCS and pen/strep) and added to the small compartment of a CL 1000 flask (CELLine). The nutrient compartment was filled with 1 liter of nutrient medium (RPMI 1640; 5% FCS and pen/strep). After incubation for 1 wk at 37°C, cells were harvested, spun at 400 *g* for 5 min, and the supernatant was removed, before being resuspended in 15 ml RF10 and returned to the cell compartment after the removal of the nutrient medium. This was replaced with 1 liter of RPMI and pen/strep, and no serum was added to encourage the virus release.

On day 16, the cells were harvested and spun at 450 *g* for 20 min. The supernatant was collected and was spun again at 450 *g* for 20 min. The supernatant was then passed through a 0.45-µm filter and stored at −80°C.

5×10^6 PBMCs were pelleted and 200 µl of EBV viral supernatant was added, followed by 1.8 ml of RF10 with 1 µg/ml of ciclosporin to prevent cytotoxic T cell killing. 5×10^5 cells (200 µl) were cultured in five wells of a 96-well plate. An additional 1 ml of RF10 with ciclosporin was added to the remaining cells, and 200 µl was plated in 10 more wells. After 7 d, 100 µl of medium in each well was replaced with fresh RF10. The culture was monitored and the medium replaced once it had turned yellow, until the point was reached where this was required every day and large cell clumps could be clearly seen. Then three wells were combined into one well of a 24-well plate with 1.4 ml of RF10. Again, these were expanded until the media needed to be replaced daily, and then transferred to a T25 with 5 ml RF10 and 100 µM acyclovir to kill any remaining virus. RF10 and acyclovir was added every 4–5 d and after 1–2 wk, transferred to a T75. These were split every 4–5 d.

F-actin quantification by flow cytometry

Flow cytometry of F-actin was performed in moDCs; CD14-negative lymphocytes; and B-LCLs from patient IV-4, and healthy controls. Patient and control cells were stained concurrently to control for any potential differences arising during the staining process. One population was labeled with a cell tracker (carboxyfluorescein succinimidyl ester [CFSE] or Dichloro-Dimethylacridin-2-One succinimidyl ester [DDAO-SE]; Molecular Probes) for 15 min in RPMI at 37°C, whereas the other was incubated in RPMI alone. This was performed reciprocally. Cells were fixed in 4% PFA for

20 min, during which time the populations were mixed, then permeabilized with 0.1% Triton X-100 for 5 min. Cells were incubated with phalloidin conjugated to Alexa Fluor-488 (DDAO) or Alexa Fluor-647 (CFSE; Molecular Probes) diluted 1/200 in PBS for 45 min and analyzed using the CyAn ADP Analyzer (Beckman Coulter).

Confocal microscopy of moDCs

100,000 moDCs were seeded onto coverslips coated in poly L-lysine and allowed to settle for 45 min. These were fixed with 4% PFA for 20 min, and then permeabilized with 0.5% triton X for 5 min. After this, nonspecific binding was blocked with donkey serum for 1 h. Coverslips were then incubated with goat anti-WDR1 (Santa Cruz Biotechnology) and rabbit anti-vinculin (Abcam) for 45 min, and, subsequently, Alexa Fluor-568 anti-rabbit and Alexa Fluor-647 anti–goat secondaries plus phalloidin-488 (Life Technologies). These were mounted with aquapolymount and imaged using the LSM 710 confocal microscope (ZEISS) with 63× objective (Plan-Apochromat; numerical aperture, 1.4; working distance, 190 µm; imaging medium, oil) with Zen2009 software (ZEISS).

WDR1 mRNA cloning

RNA was extracted from control and patient IV-4 B-LCL using TRIzol (Invitrogen) as per the manufacturer's instructions, and reverse transcribed with the high-capacity RNA to cDNA kit (Applied Biosystems). *WDR1* transcript was PCR amplified, and restriction sites were added using Phusion high fidelity polymerase (NEB), and the following primers: forward (XhoI) 5′-CGCTCGAGATGCCGTACGAGATCA AG-3′; and reverse (BamHI) 5′-CCGGATCCTCTGAGG TGATTGTCC-3′. The resultant PCR product was digested with FastDigest BamHI and XhoI (Thermo Fisher Scientific) for 15 min at 37°C. The pmCherry-N1 plasmid was also digested with BamHI and XhoI. The digests were size-selected on a 0.7% TAE agarose gel and purified using the minelute gel extraction kit (QIAGEN). 50 ng of plasmid was annealed with 60 ng PCR insert (a molar ratio of 1:3) using T4 DNA ligase (NEB). This was transformed into TOP10 (Invitrogen) chemically competent *E. coli* as per the manufacturer's instructions and plated onto Luria Broth (LB) plates containing 100 µg/ml ampicillin (Sigma-Aldrich) and grown at 37°C overnight. Six colonies of control and patient sequence were grown overnight in 5 ml of LB containing ampicillin, and the plasmid was purified using QIAprep spin miniprep kit (QIA GEN), as per the manufacturer's instructions. One plasmid containing wild-type *WDR1* sequence and one plasmid containing the *WDR1* sequence from patient IV-4 were selected for sequencing and grown in large culture for maxiprep using the GenElute HP maxiprep kit (Sigma-Aldrich). Each of these were transfected into HEK293T cells.

Reverse transfection of HEK293T cells

1 µg of the relevant WDR1-containing plasmid was added per transfection to 50 µl of opti-MEM (Gibco) and 3 µl of FuGENE HD (Promega), and incubated for 10 min before dispensing into a 24-well plate. 100,000 HEK293T cells in 500 µl RPMI with 10% FCS were then added and incubated for 24 h before imaging with a fluorescent microscope. For the double transfection, 1 µg of GFP-tagged pyrin in the pCMV6-AC-GFP vector (OriGene) was included in the transfection. The cells were seeded on polylysine-coated coverslips, and, after 24 h, were fixed with 4% PFA for 20 min and mounted with DAPI containing anti-fade mounting medium (VECTASHIELD). Z-stacks through cells were imaged using the LSM 710 (ZEISS) confocal microscope as described for moDCs.

Measurement of cytokines

IL-1β and IL-18 cytokine levels were measured in the serum of patients and controls, and in supernatants of in vitro experiments using the ready-set-go human IL-1β ELISA kit (eBioscience), and IL-18 instant ELISA kit (eBioscience) as per the manufacturer's instructions. IL-18 was also measured using a Meso Scale Discovery (MSD) multiplex kit (Meso Scale Diagnostics), as per the manufacturer's instructions in patients, controls, and sJIA patients. IL-18BP was measured using ELI SA (R&D Systems) following the manufacturer's method. Control sera was obtained from healthy pediatric controls obtained for the development of diagnostic tests for primary immunodeficiency (REC reference 06/Q0508/16; $n = 22$; 13 males; median age, 5 yr; range, 0.3–16 yr). Sera was obtained from six sJIA patients ($n = 6$; three males; median age, 11.5 yr; range, 6–15 yr; two with active disease, all on treatment).

Caspase-1 activity

PBMCs were obtained from patients CAPS ($n = 5$; three males; median age, 3 yr; range, 2.5–7.3 yr; 1 with chronic infantile neurological and cutaneous (CINCA) syndrome; and 4 with Muckle Wells Syndrome; CAPS disease activity score median 1/20, range 0–4/20; all treated with canakinumab); and from four healthy adult controls.

PBMCs were seeded in a 96-well plate at a density of 1.6×10^5 cells/well (8.0×10^5 cells/ml). Relevant wells were primed with 100 ng/ml LPS for 4 h, and, if required, then stimulated with 5 mM ATP for 30 min. Additional wells were treated with 2 µM staurosporine for 4 h as positive control. Caspase-1 activity was measured using FLICA (ImmunoChemistry Technologies), a cell-permeable fluorescent probe (FAM-YVAD-FMK) that binds active caspase-1. Cells were incubated for 1 h with FLICA at 37°C and stained with PE-conjugated anti-CD14 (BD) to identify monocytes. The gating strategy consisted of including live $CD14^+$ cells, which were subsequently analyzed for the frequency of $FLICA^+$ cells.

DC phagocytosis assay

moDCs were resuspended at 5×10^5/ml in RPMI and 10% FCS. moDCs (100 µl) were then co-cultured with an FITC-labeled unencapsulated mutant of *N. meningitidis* H44/76 (*siaD*), at a multiplicity of infection of 100. Cells

were then incubated for 4 h at 37°C, and then harvested after a series of PBS washes. The residual cell pellet was vortexed, and 20 µl was spotted onto adhesion slides (VWR) and left for 10 min to adhere, washed with PBS, and fixed for 10 min in 4% PFA. Slides were stored at −20°C until staining with 10 mg/ml P1.7 antibodies specific for *N. meningitidis* H44/76 (NIBSC), followed by Alexa Fluor 568 goat anti–mouse IgG (Life Technologies) and TO-PRO-3 (Molecular Probes; Jones et al., 2007).

The proportion of moDCs that were undergoing phagocytosis was calculated from fields of cells containing at least eight nuclei. A phagocytic event was scored a FITC cluster near the nucleus in the absence of the red P1.7 signal.

Neutrophil migration assay

Coverslips were coated with a 25 mg/ml fibrinogen for 1 h at 37°C, and then washed twice with PBS. 10^5 neutrophils were left to adhere to the coated coverslip for 30 min. The coverslip was then washed once with medium. A chemokine gradient was established within the Dunn chamber by filling the outside well with 80 µl of 1% agarose gel containing 100 nM formyl methionyl leucyl phenylalanine chemokine and leaving it to polymerize for 2 min. The inner well was filled with 50 µl of the media without chemokine, and then the chamber was completed, placing the coverslip with the neutrophils over the top. The chamber was then sealed with wax. Migration was imaged at 37°C on an Axiovert 135 microscope (ZEISS) equipped with a motorized stage that captured one image per minute for 1 h. The movie was quantified by using ImageJ (National Institutes of Health) and Ibidi analysis software. Velocity is the mean of all the instantaneous velocities (ratio between the distance d and time t) between two successive time points: $v = 1(n - 1)\ \Sigma\ ((d(pi, pi + 1))/(\Delta t))$ $n - 1\ i = 1$. Chemotactic index (CI) is the ratio between the net distance (direct distance between the starting point and the ending point) and the total distance (sum of distances the cell traveled between two time points): $CI = d(p1, pn)\ \Sigma$ $d(n - 1\ i = 1\ pi/, pi + 1)$. The instantaneous angle is the angle between the direction of the chemoattractant gradient and the direction traveled by the cell between two time points: $\alpha i = arc\ tan((yi + 1\ 2\ yi)(xi + 1\ 2\ pi))$.

shRNA-mediated knock-down of *WDR1* in THP1 cells

Six lentiviral shRNAs against *WDR1* were ordered from Open Biosystems pGIPZ shRNAmir library through the UCL RNAi core. Virus was produced in HEK293T cells and used to transduce into the THP1 monocytic cell line, as previously described (Naldini et al., 1996). Stably transduced lines were obtained using selection with Puromycin. Knock-down of *WDR1* was validated by Western blot.

Statistical analyses

All statistics (ANOVA and unpaired Student's t tests) and graphs were produced using Prism version 4 (GraphPad). $P > 0.05$ was considered significant.

Online supplemental material

Fig. S1 provides additional examples of microscopy images of moDCs and transfected 293T HEK cells shown in Fig. 3. Fig. S2 shows the phenotype in heterozygous individuals and in THP1 cells with *WDR1* knockdown did not differ from wild-type in several parameters. Table S1 elucidates in more detail the treatments and immunological tests received by the two patients. Regions of genetic homozygosity found in both of these patients and not in the siblings or parents are listed in Table S2.

ACKNOWLEDGMENTS

This work was funded by the Nuffield Foundation Oliver Bird program and the Rosetrees Trust (A.S.I. Standing). D. Malinova was supported by the Child Health Research Appeal, and J. Record was supported by University College London Grand Challenge Studentship. A.J. Thrasher is supported by both the Wellcome Trust (104807/Z/14/Z; along with D. Moulding and M.P. Blundell) and by the National Institute for Health Research Biomedical Research Centre at Great Ormond Street Hospital for Children NHS Foundation Trust and University College London.

The authors declare no competing financial interests.

Submitted: 1 August 2016
Revised: 11 October 2016
Accepted: 29 November 2016

REFERENCES

Adzhubei, I.A., S. Schmidt, L. Peshkin, V.E. Ramensky, A. Gerasimova, P. Bork, A.S. Kondrashov, and S.R. Sunyaev. 2010. A method and server for predicting damaging missense mutations. *Nat. Methods.* 7:248–249. http://dx.doi.org/10.1038/nmeth0410-248

Allen, R.C., R.J. Armitage, M.E. Conley, H. Rosenblatt, N.A. Jenkins, N.G. Copeland, M.A. Bedell, S. Edelhoff, C.M. Disteche, D.K. Simoneaux, et al. 1993. CD40 ligand gene defects responsible for X-linked hyper-IgM syndrome. *Science.* 259:990–993. http://dx.doi.org/10.1126/science.7679801

Bode, S.F.N., K. Lehmberg, A. Maul-Pavicic, T. Vraetz, G. Janka, U.Z. Stadt, and S. Ehl. 2012. Recent advances in the diagnosis and treatment of hemophagocytic lymphohistiocytosis. *Arthritis Res. Ther.* 14:213. http://dx.doi.org/10.1186/ar3843

Bouma, G., A. Mendoza-Naranjo, M.P. Blundell, E. de Falco, K.L. Parsley, S.O. Burns, and A.J. Thrasher. 2011. Cytoskeletal remodeling mediated by WASp in dendritic cells is necessary for normal immune synapse formation and T-cell priming. *Blood.* 118:2492–2501. http://dx.doi.org/10.1182/blood-2011-03-340265

Brydges, S.D., L. Broderick, M.D. McGeough, C.A. Pena, J.L. Mueller, and H.M. Hoffman. 2013. Divergence of IL-1, IL-18, and cell death in NLRP3 inflammasomopathies. *J. Clin. Invest.* 123:4695–4705. http://dx.doi.org/10.1172/JCI71543

Calvez, R., F. Lafouresse, J. De Meester, A. Galy, S. Valitutti, and L. Dupré. 2011. The Wiskott-Aldrich syndrome protein permits assembly of a focused immunological synapse enabling sustained T-cell receptor signaling. *Haematologica.* 96:1415–1423. http://dx.doi.org/10.3324/haematol.2011.040204

Canna, S.W., A.A. de Jesus, S. Gouni, S.R. Brooks, B. Marrero, Y. Liu, M.A. DiMattia, K.J.M. Zaal, G.A.M. Sanchez, H. Kim, et al. 2014. An activating NLRC4 inflammasome mutation causes autoinflammation with recurrent macrophage activation syndrome. *Nat. Genet.* 46:1140–1146. http://dx.doi.org/10.1038/ng.3089

Cervero, P., M. Himmel, M. Krüger, and S. Linder. 2012. Proteomic analysis of podosome fractions from macrophages reveals similarities to spreading initiation centres. *Eur. J. Cell Biol.* 91:908–922. http://dx.doi.org/10.1016/j.ejcb.2012.05.005

Chen, O., N. Shan, X. Zhu, Y. Wang, P. Ren, D. Wei, and R. Sun. 2013. The imbalance of IL-18/IL-18BP in patients with systemic juvenile idiopathic arthritis. *Acta Biochim. Biophys. Sin. (Shanghai).* 45:339–341. http://dx.doi.org/10.1093/abbs/gmt007

Dinarello, C.A., D. Novick, S. Kim, and G. Kaplanski. 2013. Interleukin-18 and IL-18 binding protein. *Front. Immunol.* 4:289. http://dx.doi.org/10.3389/fimmu.2013.00289

Dupré, L., A. Aiuti, S. Trifari, S. Martino, P. Saracco, C. Bordignon, and M.G. Roncarolo. 2002. Wiskott-Aldrich syndrome protein regulates lipid raft dynamics during immunological synapse formation. *Immunity.* 17:157–166.

Flannagan, R.S., V. Jaumouillé, K.K. Huynh, J.D. Plumb, G.P. Downey, M.A. Valvano, and S. Grinstein. 2012. Burkholderia cenocepacia disrupts host cell actin cytoskeleton by inactivating Rac and Cdc42. *Cell. Microbiol.* 14:239–254. http://dx.doi.org/10.1111/j.1462-5822.2011.01715.x

Frenkel, J. 2014. Autoinflammation and immunodeficiency. *Pediatr. Rheumatol. Online J.* 12:I34. http://dx.doi.org/10.1186/1546-0096-12-S1-I34

Gavrilin, M.A., D.H.A. Abdelaziz, M. Mostafa, B.A. Abdulrahman, J. Grandhi, A. Akhter, A. Abu Khweek, D.F. Aubert, M.A. Valvano, M.D. Wewers, and A.O. Amer. 2012. Activation of the pyrin inflammasome by intracellular *Burkholderia cenocepacia*. *J. Immunol.* 188:3469–3477. http://dx.doi.org/10.4049/jimmunol.1102272

Hagar, J.A., D.A. Powell, Y. Aachoui, R.K. Ernst, and E.A. Miao. 2013. Cytoplasmic LPS activates caspase-11: implications in TLR4-independent endotoxic shock. *Science.* 341:1250–1253. http://dx.doi.org/10.1126/science.1240988

Hu, K.H., and M.J. Butte. 2016. T cell activation requires force generation. *J. Cell Biol.* 213:535–542. http://dx.doi.org/10.1083/jcb.201511053

Jones, H.E., H. Uronen-Hansson, R.E. Callard, N. Klein, and G.L.J. Dixon. 2007. The differential response of human dendritic cells to live and killed *Neisseria meningitidis*. *Cell. Microbiol.* 9:2856–2869. http://dx.doi.org/10.1111/j.1462-5822.2007.01001.x

Jones, H.E., J. Strid, M. Osman, H. Uronen-Hansson, G. Dixon, N. Klein, S.Y.C. Wong, and R.E. Callard. 2008. The role of beta2 integrins and lipopolysaccharide-binding protein in the phagocytosis of dead *Neisseria meningitidis*. *Cell. Microbiol.* 10:1634–1645. http://dx.doi.org/10.1111/j.1462-5822.2008.01154.x

Kile, B.T., A.D. Panopoulos, R.A. Stirzaker, D.F. Hacking, L.H. Tahtamouni, T.A. Willson, L.A. Mielke, K.J. Henley, J.G. Zhang, I.P. Wicks, et al. 2007. Mutations in the cofilin partner Aip1/Wdr1 cause autoinflammatory disease and macrothrombocytopenia. *Blood.* 110:2371–2380. http://dx.doi.org/10.1182/blood-2006-10-055087

Kim, M.L., J.J. Chae, Y.H. Park, D. De Nardo, R.A. Stirzaker, H.J. Ko, H. Tye, L. Cengia, L. DiRago, D. Metcalf, et al. 2015. Aberrant actin depolymerization triggers the pyrin inflammasome and autoinflammatory disease that is dependent on IL-18, not IL-1β. *J. Exp. Med.* 212:927–938. http://dx.doi.org/10.1084/jem.20142384

Li, J., W.M. Brieher, M.L. Scimone, S.J. Kang, H. Zhu, H. Yin, U.H. von Andrian, T. Mitchison, and J. Yuan. 2007. Caspase-11 regulates cell migration by promoting Aip1-Cofilin-mediated actin depolymerization. *Nat. Cell Biol.* 9:276–286. http://dx.doi.org/10.1038/ncb1541

Malinova, D., M. Fritzsche, C.R. Nowosad, H. Armer, P.M.G. Munro, M.P. Blundell, G. Charras, P. Tolar, G. Bouma, and A.J. Thrasher. 2016. WASp-dependent actin cytoskeleton stability at the dendritic cell immunological synapse is required for extensive, functional T cell contacts. *J. Leukoc. Biol.* 99:699–710

Mohri, K., S. Vorobiev, A.A. Fedorov, S.C. Almo, and S. Ono. 2004. Identification of functional residues on *Caenorhabditis elegans* actin-interacting protein 1 (UNC-78) for disassembly of actin depolymerizing factor/cofilin-bound actin filaments. *J. Biol. Chem.* 279:31697–31707. http://dx.doi.org/10.1074/jbc.M403351200

Moulding, D.A., J. Record, D. Malinova, and A.J. Thrasher. 2013. Actin cytoskeletal defects in immunodeficiency. *Immunol. Rev.* 256:282–299. http://dx.doi.org/10.1111/imr.12114

Naldini, L., U. Blömer, P. Gallay, D. Ory, R. Mulligan, F.H. Gage, I.M. Verma, and D. Trono. 1996. In vivo gene delivery and stable transduction of nondividing cells by a lentiviral vector. *Science.* 272:263–267. http://dx.doi.org/10.1126/science.272.5259.263

Okada, K., T. Obinata, and H. Abe. 1999. XAIP1: a *Xenopus* homologue of yeast actin interacting protein 1 (AIP1), which induces disassembly of actin filaments cooperatively with ADF/cofilin family proteins. *J. Cell Sci.* 112:1553–1565.

Okada, K., L. Blanchoin, H. Abe, H. Chen, T.D. Pollard, and J.R. Bamburg. 2002. *Xenopus* actin-interacting protein 1 (XAip1) enhances cofilin fragmentation of filaments by capping filament ends. *J. Biol. Chem.* 277:43011–43016. http://dx.doi.org/10.1074/jbc.M203111200

Okreglak, V., and D.G. Drubin. 2007. Cofilin recruitment and function during actin-mediated endocytosis dictated by actin nucleotide state. *J. Cell Biol.* 178:1251–1264. http://dx.doi.org/10.1083/jcb.200703092

Ono, S., K. Mohri, and K. Ono. 2004. Microscopic evidence that actin-interacting protein 1 actively disassembles actin-depolymerizing factor/Cofilin-bound actin filaments. *J. Biol. Chem.* 279:14207–14212. http://dx.doi.org/10.1074/jbc.M313418200

Orange, J.S., A. Jain, Z.K. Ballas, L.C. Schneider, R.S. Geha, and F.A. Bonilla. 2004. The presentation and natural history of immunodeficiency caused by nuclear factor kappaB essential modulator mutation. *J. Allergy Clin. Immunol.* 113:725–733. http://dx.doi.org/10.1016/j.jaci.2004.01.762

Rodal, A.A., J.W. Tetreault, P. Lappalainen, D.G. Drubin, and D.C. Amberg. 1999. Aip1p interacts with cofilin to disassemble actin filaments. *J. Cell Biol.* 145:1251–1264. http://dx.doi.org/10.1083/jcb.145.6.1251

Rosales-Reyes, R., A.M. Skeldon, D.F. Aubert, and M.A. Valvano. 2012. The Type VI secretion system of Burkholderia cenocepacia affects multiple Rho family GTPases disrupting the actin cytoskeleton and the assembly of NADPH oxidase complex in macrophages. *Cell. Microbiol.* 14:255–273. http://dx.doi.org/10.1111/j.1462-5822.2011.01716.x22023353

Sarrauste de Menthière, C., S. Terrière, D. Pugnère, M. Ruiz, J. Demaille, and I. Touitou. 2003. INFEVERS: the Registry for FMF and hereditary inflammatory disorders mutations. *Nucleic Acids Res.* 31:282–285. http://dx.doi.org/10.1093/nar/gkg031

Sasahara, Y., R. Rachid, M.J. Byrne, M.A. de la Fuente, R.T. Abraham, N. Ramesh, and R.S. Geha. 2002. Mechanism of recruitment of WASP to the immunological synapse and of its activation following TCR ligation. *Mol. Cell.* 10:1269–1281. http://dx.doi.org/10.1016/S1097-2765(02)00728-1

Savina, A., and S. Amigorena. 2007. Phagocytosis and antigen presentation in dendritic cells. *Immunol. Rev.* 219:143–156. http://dx.doi.org/10.1111/j.1600-065X.2007.00552.x

Schwarz, J.M., C. Rödelsperger, M. Schuelke, and D. Seelow. 2010. MutationTaster evaluates disease-causing potential of sequence alterations. *Nat. Methods.* 7:575–576. http://dx.doi.org/10.1038/nmeth0810-575

Shi, J., Y. Zhao, Y. Wang, W. Gao, J. Ding, P. Li, L. Hu, and F. Shao. 2014. Inflammatory caspases are innate immune receptors for intracellular LPS. *Nature.* 514:187–192. http://dx.doi.org/10.1038/nature13683

Standing, A., E. Omoyinmi, and P. Brogan. 2013. Gene hunting in autoinflammation. *Clin. Transl. Allergy.* 3:32. http://dx.doi.org/10.1186/2045-7022-3-32

Vastert, S.J., W. de Jager, B.J. Noordman, D. Holzinger, W. Kuis, B.J. Prakken, and N.M. Wulffraat. 2014. Effectiveness of first-line treatment with

recombinant interleukin-1 receptor antagonist in steroid-naive patients with new-onset systemic juvenile idiopathic arthritis: results of a prospective cohort study. *Arthritis Rheumatol.* 66:1034–1043. http://dx.doi.org/10.1002/art.38296

Waite, A.L., P. Schaner, C. Hu, N. Richards, B. Balci-Peynircioglu, A. Hong, M. Fox, and D.L. Gumucio. 2009. Pyrin and ASC co-localize to cellular sites that are rich in polymerizing actin. *Exp. Biol. Med. (Maywood).* 234:40–52. http://dx.doi.org/10.3181/0806-RM-184

Wheeler, R.D., C.M. Cale, V. Cetica, M. Aricò, and K.C. Gilmour. 2010. A novel assay for investigation of suspected familial haemophagocytic lymphohistiocytosis. *Br. J. Haematol.* 150:727–730. http://dx.doi.org/10.1111/j.1365-2141.2010.08289.x

Xu, H., J. Yang, W. Gao, L. Li, P. Li, L. Zhang, Y.N. Gong, X. Peng, J.J. Xi, S. Chen, et al. 2014. Innate immune sensing of bacterial modifications of Rho GTPases by the Pyrin inflammasome. *Nature.* 513:237–241. http://dx.doi.org/10.1038/nature13449